Hydrodynamic rotlet dipole driven by spinning chiral liquid crystal droplets

Takaki Yamamoto[1,*] and Masaki Sano[2,†]

[1]*Laboratory for Physical Biology, RIKEN Center for Biosystems Dynamics Research, Kobe 650-0047, Japan*

[2]*Department of Physics, Universal Biology Institute, The University of Tokyo, 7-3-1 Hongo, Bunkyo-ku, Tokyo 113-0033, Japan*

(Received 22 December 2018; published 25 February 2019)

Chirality is an essential evolutionary-conserved physical aspect of swimming microorganisms. However, the role of chirality on the hydrodynamics of such microswimmers is still being elucidated. Hydrodynamic theories have so far predicted that, under a torque-free condition satisfied in the system of microswimmers, a rotlet dipole generating a twisting flow is the leading-order singularity of the chiral flow field. Nevertheless, such a chiral flow field has never been experimentally detected. Here we explore a hydrodynamic field generated in a system of a chiral microswimmer, where a droplet of a cholesteric liquid crystal (CLC) exhibits helical and spinning motions in surfactant solutions due to a chiral nonequilibrium cross coupling between the rotation and the Marangoni flow. Combining measurement of the flow field around the spinning CLC droplets and a computational flow modeling, we revealed that the CLC droplets generate a flow field of a rotlet dipole. Remarkably, we found that the chiral component of the flow field decays with distance r as r^{-3}, which is consistent with the theoretical prediction for the flow field produced by a point singularity of a rotlet dipole. Our findings will promote the understanding of roles of chirality on the hydrodynamics in active matter as well as liquid crystals.

DOI: 10.1103/PhysRevE.99.022704

I. INTRODUCTION

Collective motions of swimming microorganisms, such as swarming [1–5], formation of biofilm [6,7], and bacterial turbulence [8,9], are so ubiquitous in nature that the mechanism is now of great interest but still being elucidated. Such collective behaviors emerge from physical interactions as well as biochemical cues. For the physical understanding of the mechanism of the collective behaviors of the swimming microorganisms, it is essential to reveal the hydrodynamic interaction between them. Flow fields around swimming microorganisms have been theoretically analyzed by models such as a superposition of singularity solutions of the Stokes equation [10,11] and squirmer models [12–14]. Many of these theoretical studies suggested the importance of a flow field of a force dipole, which classifies the swimming microorganisms into a pusher and a puller type [13] and qualitatively alters the hydrodynamic interaction and so collective behaviors [15,16]. Experimental studies have also revealed the existence of force dipoles in the hydrodynamic field generated by a variety of microorganisms such as *Volvox carteri* [17], *Chlamydomonas reinhardtii* [17], and *Escherichia coli* [18].

In contrast to such achiral flow fields characterized by force dipoles, chiral rotational flow fields generated by swimming microorganisms are less understood, whereas most of the microorganisms show chiral motions such as spinning [19,20], circular [10,21], and helical motions [22,23], owing to their chiral cell bodies. Drescher *et al.* reported that *Volvox carteri* spins near the glass-water boundary using their flagellar at the body surface, and a pair of them show an oscillatory motion due to the hydrodynamic interaction [19]. Petroff *et al.* reported that *Thiovulum majus*, a bacterium swimming by rotating its flagella, produces rotating flow and accumulates collectively near the glass surface to form a hexagonal lattice reorganizing dynamically [20]. However, the chiral rotational flow around such spinning microorganisms has not been experimentally quantified.

In general, under a torque-free condition satisfied when a microorganism swims freely, a flow field characterized by a rotlet dipole should appear as the leading-order effect [13,14]. In a recent theoretical study, Tjhung *et al.* emphasized the importance of the effect of the rotlet dipole on the dynamics of microswimmers by reporting that a droplet filled with a chiral active gel generating torque dipole exhibits helical and other chiral motions [24]. In this study, we experimentally report that a flow field characterized by a rotlet dipole appears in our experimental system of a chiral microswimmer which satisfies a torque-free condition.

We recently developed an experimental system of an artificial chiral microswimmer, in which droplets of cholesteric liquid crystal (CLC), a chiral phase of liquid crystal, swim in helical paths in surfactant solutions [25]. The experimental system is an ideal model system of chiral microswimmers, since the strength of both chirality and self-propulsion can be experimentally controlled by altering the concentration of the chiral dopant and the surfactant solution. In the experimental system, the dissolution process of the CLC molecules into the surfactant solutions spontaneously induces the gradient of the surface tension on the interface of the droplet and so the Marangoni flow. Due to a nonequilibrium cross coupling between the Marangoni flow and the rotation of the CLC droplet via the helical director field, the CLC droplets exhibit helical motion. While we proposed a phenomenological model of the spontaneous helical motion based on a particle model [26],

*takaki.yamamoto@riken.jp

†sano@daisy.phys.s.u-tokyo.ac.jp

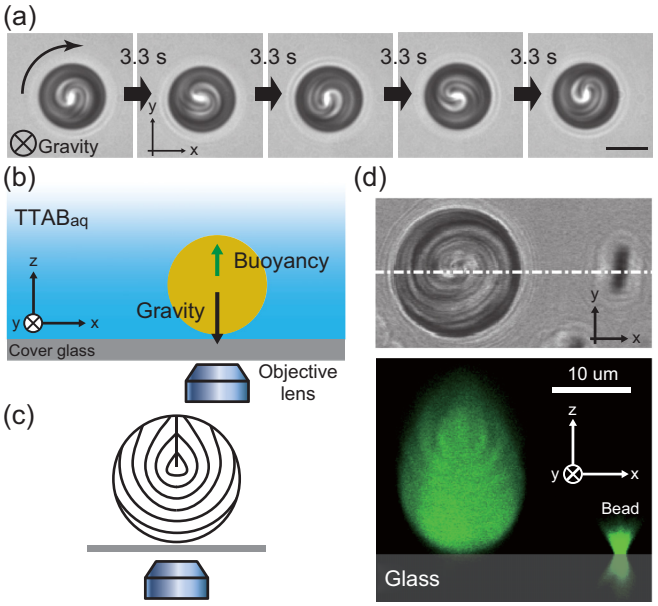

FIG. 1. Rotating behavior of a CLC droplet and the experimental setup. (a) A rotating spiral texture of a CLC droplet. A curved arrow indicates the rotational direction (CW). The scale bar is 10 μm. (b) The rotating behavior of a CLC droplet in a surfactant solution was observed after the droplet sank to the bottom of the chamber. (c) A schematic of a cross-sectional view of the director field inside a CLC droplet with a spiral texture. A solid line represents a disclination line. (d) Confocal observation of a cross-sectional view of a CLC droplet with a spiral texture. The top and bottom figures show the cross-sectional images in the xy plane (transmitted light image) and xz plane (fluorescent confocal image). The dashed line in the xy plane indicates the position of the xz plane. The position of the cover glass detected by a fluorescent bead attached to the surface is also shown. The scale bar is 10 μm.

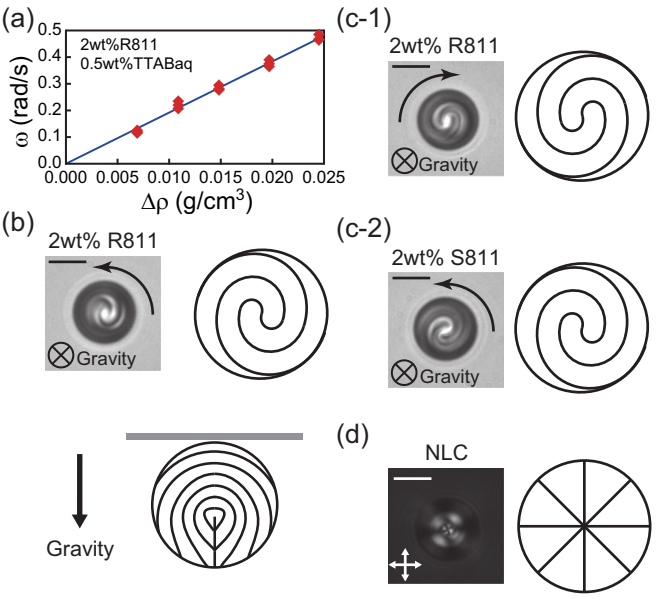

FIG. 2. Angular velocity of rotating CLC droplets, and texture of CLC droplets with opposite handedness and a NLC droplet. (a) Angular velocity ω of the rotating spiral texture of the CLC droplets ($D \approx 16$ μm) vs density difference $\Delta\rho$ between the surfactant solution and the CLC. The blue solid line is a linear fit to the data. (b) The texture of the CLC droplets doped with R811 when $\Delta\rho < 0$. The droplet floats at the top glass of the chamber. The curved arrows indicate the rotational direction. (c) The texture of the CLC droplets doped with chiral dopants which have opposite chirality [(c-1) R811 and (c-2) S811], respectively. (d) A nonrotating texture of a NLC droplet observed under crossed polarizers. The direction of the crossed polarizers are shown as a pair of the double-headed arrows. A cross-sectional view of the radial director field inside the NLC droplet is also schematically drawn. The scale bars in panels (b), (c), and (d) are 10 μm.

the mechanism of the chiral motion is still being elucidated from the view point of hydrodynamics, due to the difficulty in measuring the flow field around the CLC droplets moving around in three dimensions.

In this study, we investigate a rotational flow generated by the CLC droplets by realizing a situation in which the CLC droplets exhibit a spinning motion. We discovered that the spiral texture of the CLC droplet in the surfactant solution rotates unidirectionally without the displacement of the center of mass, after the droplet sinks to the bottom of the chamber as shown in Figs. 1(a) and 1(b). Since the rotational velocity was proportional to the density difference between the surfactant solution and the CLC [Fig. 2(a)], the spatial gradient of the surfactant concentration induced by the density difference is the driving force of the spinning motion. Hence, the experimental setup enables us to investigate the flow field around the CLC droplets under the gradient of surfactant concentration, which is the origin of the self-propulsion of the CLC droplets. In this experimental setup, we investigated a three-dimensional (3D) hydrodynamic flow around the spinning CLC droplets by particle image velocimetry (PIV) using a confocal microscope. We surprisingly found that a "twisting flow" [see Fig. 5(b)], a feature of a flow field of a rotlet dipole, is generated around the CLC droplets. Furthermore, we numerically confirmed that a spherical squirmer model with a surface flow represented by a rotlet dipole provides a good approximation of the twisting flow around the CLC droplets.

II. RESULTS

A. Rotation of the CLC droplets with spiral pattern

We observed a continuously rotating spiral texture of a microscale CLC droplet (diameter $D = 10$–30 μm) in an aqueous surfactant solution [Fig. 1(a); see Movie S1 [27]], after the droplet was injected using a micro-injector (Femtojet) and then sank to the bottom of a sample chamber as shown in Fig. 1(b) (see Appendix A). We used a mixture of a nematic liquid crystal (NLC) [5CB (4-cyano-4′-pentylbiphenyl)] and 2wt% of a chiral dopant (R811) as the CLC, and 0.5wt% of TTAB (tetradecyltrimethylammonium bromide) as the surfactant, unless otherwise noted. As indicated by a fourfold symmetric texture of a NLC droplet under crossed polarizers shown in Fig. 2(d), with which the NLC droplet has a radial director field with a point defect at the center, the anchoring condition of the LC droplets in TTAB solution is homeotropic.

It has been reported that a spiral texture of a CLC droplet is observed when the droplet has the director field called radial spherical structure (RSS) [28–30], in which the droplet has a radial disclination line originating from the center of the droplet and pointing to its surface, and parallel to the optical axis [Fig. 1(c)]. Although the RSS is defined for the CLC droplets under planar anchoring conditions [28–30], the CLC droplets under homeotropic anchoring conditions also exhibit the spiral pattern with the similar director field to the RSS [31]. However, due to the constraint of homeotropic anchoring conditions, additional surface defects should exist in addition to the radial disclination line in the RSS as discussed in Ref. [31]. Therefore, we consider that our CLC droplets with spiral pattern have the "RSS-like structure," which is with the director field similar to the RSS inside the droplet and additional defects at the interface.

For further characterization of the structure of the CLC droplet, we observed the cross-sectional texture of the droplet using a confocal microscope (TCS SP5, Leica) with a 40× oil immersion objective (HCX PL APO) by adding a small amount of fluorescent dye [0.01wt% of N,N-bis(2,5-di-tert-butylphenyl)-3,4,9,10- perylenedicarboximide (BTBP)] into the CLC as shown in Fig. 1(d). Here we detected the surface of the bottom glass by fluorescent beads (FluoSpheres amine-modified microspheres, yellow-green, 1.0 μm, Thermo Fisher Scientific) attached to the glass surface. We clearly found that the droplet is not in contact with the cover glass. Furthermore, we consider that the downward convex layers observed in Fig. 1(d) indicate that the droplet is the RSS-like structure with a disclination line located in the semisphere far from the objective lens as depicted in Fig. 1(c). The LC pattern in the semisphere far from the objective lens is inevitably blurred by lensing due to the birefringence of the LC.

As shown in Fig. 1(a), we found that the rotation of the spiral texture was always in the clockwise (CW) direction. We thus suspected that the rotation is driven by a nonequilibrium cross coupling, allowed in chiral systems, between the rotation of the CLC droplet and the gravity, which is an only external field in our system. To investigate the effect of the gravity on the rotation, we controlled the buoyant force exerted on the CLC droplet by partly replacing H_2O with D_2O (deuterium oxide). Figure 2(a) shows the angular velocity ω of the CLC droplets ($D \approx 16$ μm) for the different density differences $\Delta\rho = \rho_{\mathrm{LC}} - \rho_{\mathrm{TTAB}}$, where ρ_{LC} and ρ_{TTAB} are the density of the CLC and TTAB in D_2O/H_2O, respectively. We found that ω is proportional to $\Delta\rho$. Hence, we concluded that the driving force of the rotation is the density difference $\Delta\rho$. As shown in Fig. 2(b), we also confirmed the reversal of the direction of the rotation when the droplet floats at the top glass of the chamber in $\Delta\rho < 0$ by using only D_2O for the surfactant solution. Here we found the handedness of the spiral pattern is also reversed as opposed to that observed in $\Delta\rho > 0$. This observation means that the CLC droplet has a polar structure along the z axis. The RSS-like structure, which has a disclination line in the semisphere, is certainly polar. Since the polarity in $\Delta\rho < 0$ is reversed from that in $\Delta\rho > 0$, the disclination line should locate in the bottom semisphere when $\Delta\rho < 0$ [Fig. 2(b)].

Furthermore, we investigated the effect of the chirality of the CLC droplets on the rotation by observing the rotation of the CLC droplets doped with either 2wt% R811 or 2wt% S811, which are enantiomers and induce helical director fields with the opposite handedness on the CLC droplets. We found that the CLC droplets which have spiral patterns with opposite handedness rotate in the opposite direction as shown in Figs. 2(c-1) and 2(c-2) (see Movie S2 [27] for the S811-doped droplet). Here all the R811-doped droplets with spiral pattern ($D = 10$–30 μm) rotated in the CW direction (36 droplets), while all the S811-doped droplets rotated in the counterclockwise (CCW) direction (19 droplets). We also confirmed that the NLC droplets (5CB), which have a radial director field with a point defect at the center and exhibit a fourfold symmetric texture under crossed polarizers, do not rotate [Fig. 2(d)]. Since the chirality of the CLC determines the rotational direction, the rotation of the CLC droplets is induced by a nonequilibrium cross coupling between the rotation and the gravity, which is possible only in chiral systems.

We propose a mechanism of the rotation of the CLC droplets. In our experiments, micelles gradually dissolve the CLC molecules [25,32]. When $\Delta\rho > 0$, the micelles filled with the CLC molecules sink to the bottom of the sample chamber, and the empty micelles and free surfactant molecules are distributed with a higher concentration as the distance from the bottom increases. The free surfactant molecules should thus tend to adsorb on the upper surface of the droplet. Consequently, the surface tension gets higher at the bottom side of the droplet to pull the fluid toward the bottom. We consider that the disclination lines are dragged by the hydrodynamic flow inside the droplet and conveyed to the semisphere far from the glass surface. It is reported that the texture of the CLC rotates when subjected to external fields such as a temperature gradient [33–42]. Such rotation of the texture, the so-called Lehmann-type effect, has been explained as a result of a nonequilibrium cross coupling between the rotation and the external field only allowed in chiral systems. We consider that, also in our experiment, the fluid flow driven by the density difference couples with the chiral director field of the CLC droplets to induce the rotation of the spiral texture. Rotational behavior of CLC droplets with other textures is shown in Appendix B.

B. PIV measurement of the hydrodynamic field around the NLC and CLC droplets

To understand the mechanism of the chiral nonequilibrium cross coupling between the hydrodynamic flow and the rotation of the CLC droplet from the viewpoint of hydrodynamics, it is essential to detect the hydrodynamic field. Here we investigated the 3D hydrodynamic field around the nonrotating NLC and the rotating CLC droplets by means of PIV analysis (see Appendix C). We added fluorescent microspheres ($D =$ 1 μm) into 2wt% TTAB H_2O solution, and injected the NLC (5CB) or CLC (5CB+2wt%R811) droplets. To detect the position of the droplets, we added a small amount of a fluorescent dye (0.01wt% of BTBP) into LCs. In the PIV experiments, we injected relatively large droplets ($D = 24$ μm). With the diameter, the director fields of both of the CLC and the NLC droplets are the same as those in Figs. 2(c-1) and 2(d), respectively. To detect the hydrodynamic field at

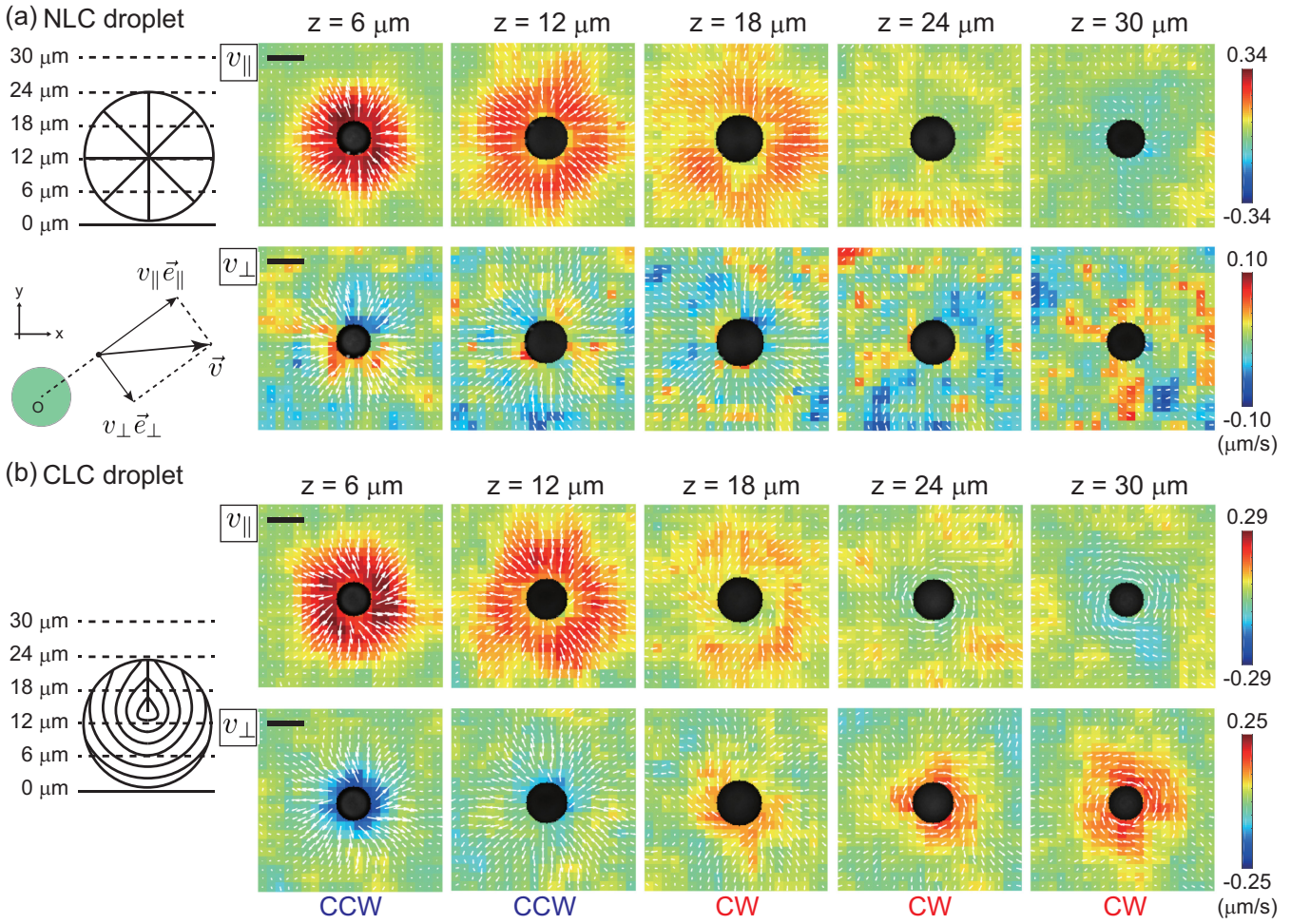

FIG. 3. Flow fields around a NLC and a CLC droplets at each height. (a)(b)The white arrows indicate the velocity vector in the xy plane. The color represents the amplitudes of $v_\parallel$ and $v_\perp$. The definition of $v_\parallel$ and $v_\perp$ is also schematically drawn in panel (a). The dark circular region at the center of each panel is the area masked to avoid the texture of the LC droplets in the PIV analysis (see Appendix C). The scale bars are 20 μm.

different heights ($z = 6, 12, 18, 24, 30$ μm) as shown in Fig. 3, we used a confocal microscope. Here $z = 0$ μm is set as the height of the glass surface on the bottom.

We obtained time-lapse images of the xy plane at each height (see Appendix C). Figures 3(a) and 3(b) show the results of the PIV analysis for the NLC and the CLC droplets, respectively. We define $v_\parallel$ and $v_\perp$ by decomposing a velocity field $\vec{v}(x, y)$ projected on the xy plane as $\vec{v}(x, y) = v_\parallel \vec{e}_\parallel + v_\perp \vec{e}_\perp$, where $\vec{e}_\parallel$ and $\vec{e}_\perp$ are unit vectors in the radial and angular directions, respectively. Here we set the origin of the xy coordinates at the center of the cross section of the droplet at each height, and $\vec{e}_\perp$ as directed in the CW direction [Fig. 3(a)]. If the flow is the outward (inward) direction, $v_\parallel$ is positive (negative). Also, if it is the CW (CCW) direction, $v_\perp$ is positive (negative). We found that the radial components $v_\parallel$ are similar in both of the NLC and the CLC droplets. In both cases, the flow is outward below $z = 18$ μm, while it is slightly inward near and above the top of the droplets. In contrast, the angular components $v_\perp$ are strikingly different in both cases. In the NLC droplets, we did not observe any significant amplitude for $v_\perp$ at every height. However, in the CLC droplets, the flow field is in the CCW direction below $z = 12$ μm, while it is in the CW direction above $z = 18$ μm. Hence, the CLC droplets produce a "twisting flow," which is reminiscent of a twisting flow of actomyosin cortex inside *Caenorhabditis elegans* embryos [43]. Since the hydrodynamic flow outside and inside the droplets should be continuous, the direction of flow inside the droplet should be the same at least near the interface as the flow outside the droplet. In contrast, the cross-sectional texture of the CLC droplets rotated in the CW direction at every height. Therefore, counterintuitively, the rotation of texture and the surface flow at the interface are not necessarily in the same direction. We will quantify this twisting flow in detail in the next section.

C. Surface flow on the NLC and the CLC droplets: Experiment and theory

The flow field in the surfactant solution measured above should be driven by a flow at the interface, which we call the surface flow. We speculate about the surface flow by

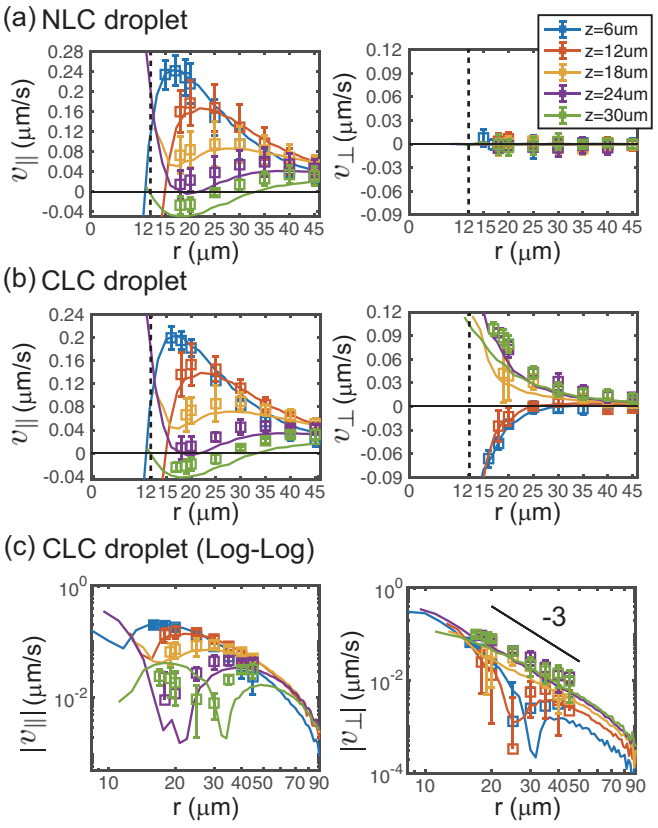

FIG. 4. The radial profiles of $v_\parallel$ and $v_\perp$ obtained from the experiments with (a) the NLC and (b, c) the CLC droplets. (a, b) The squares with the error bars indicate the experimental data. The solid curves are the numerical results. The different colors correspond to the different heights of the xy plane cross sections (blue: $z = 6$ μm, red: $z = 12$ μm, yellow: $z = 18$ μm, purple: $z = 24$ μm, green: $z = 30$ μm). The dotted lines indicate the radius of the droplets. (c) The log-log plots of $|v_\parallel|$ and $|v_\perp|$ are shown for the CLC droplets. A solid line in the plot for $|v_\perp|$ indicates a power law with an exponent -3.

investigating the profile of the flow field in the surfactant solution in more detail. Figures 4(a) and 4(b) show the radial profile of $v_\parallel$ and $v_\perp$ for the NLC and the CLC droplets, respectively. Here we calculated the radial profile using time-lapse images of z stacks ($xyzt$ data) for several droplets with $D = 24$ μm (four droplets for the CLC and five droplets for the NLC, respectively) (see Appendix C). We found that both $v_\parallel$ and $v_\perp$ decay as the distance r from the center of the droplet increases for both cases.

To elucidate what kind of a surface flow reproduces such experimentally obtained radial profiles, we apply a spherical squirmer model, which is intensively studied to calculate a flow field around a microswimmer swimming in a viscous fluid at low Reynolds number, whose dynamics is described by Stokes equation [12–14]. The spherical squirmer model assumes a surface flow on a sphere to calculate the hydrodynamic field around the sphere. Since Reynolds number Re is $O(10^{-5})$ in our experimental system, the spherical squirmer model is applicable. Following Ref. [14], we expand the surface velocity $\vec{u}(\theta, \phi)$ of the CLC droplet with a diameter D as follows:

$$\vec{u}(\theta,\phi) = \sum_{n=1}^{\infty} -\frac{2\sin\theta P_n'}{(D/2)^{n+2}n} B_{0n}\vec{e}_\theta + \sum_{n=1}^{\infty} \frac{\sin\theta P_n'}{(D/2)^{n+1}} C_{0n}\vec{e}_\phi, \tag{1}$$

where we use spherical coordinates with the origin at the center of the sphere and define $\vec{e}_\theta$ and $\vec{e}_\phi$ as the basis vectors, and θ and ϕ are the polar and the azimuthal angles, respectively. Here θ was measured from the positive z axis defined in Fig. 1(a), and we assumed the axial symmetry with respect to the z axis. $P_n = P_n(\cos\theta)$ is the Legendre polynomials of degree n, and P_n' is the derivative of P_n. The first terms on the right-hand side of Eq. (1) represent the achiral surface flow, while the last terms represent the chiral rotational surface flow.

As a first-order approximation, we consider only the lowest order modes for both the achiral and the chiral surface flow. For the achiral flow, the lowest order term is the term with the coefficient B_{01}. The term is composed of a Stokeslet and a source dipole singularities in the z direction [14]. A Stokeslet and a source dipole singularities put at the origin along the z axis induce the flow field $\vec{u}_S(r,\theta,\phi) = \alpha(2\cos\theta\vec{e}_r - \sin\theta\vec{e}_\theta)/r$ and $\vec{u}_{SD}(r,\theta,\phi) = \beta(2\cos\theta\vec{e}_r + \sin\theta\vec{e}_\theta)/r^3$, where r is the distance from the origin [14]. Therefore, superimposing the Stokeslet and source dipole with $\alpha = B_{01}/(D/2)^2$ and $\beta = -B_{01}$, we obtain the term with the coefficient B_{01} in Eq. (1) at the surface of the droplet ($r = D/2$). Note that a Stokeslet should vanish in any force-free system [13]. Nevertheless, since the LC droplets are exposed to the buoyant force and the gravity, which do not vanish in total, the B_{01} term is possible as the lowest order term. With respect to the chiral rotational flow, the term with C_{02} is the lowest order term possible in our experiments. The term with C_{01} is a rotlet singularity, which cannot exist in any torque-free system [13]. Since no external torque is imposed on our system, it is a torque-free system. The C_{02} term is composed of a rotlet dipole singularity in the z direction, which, we expected, is responsible for the twisting flow observed around the CLC droplets.

In Fig. 4 the flow field obtained by a numerical simulation (solid lines) of the Stokes equation is shown together with experimental data (squares). Here the flow field is simulated for a sphere sitting at the bottom with the surface velocity represented by the B_{01} and C_{02} terms. The 3D flow fields and streamlines around the droplets are also shown in Fig. 5. We used only the B_{01} term to model the NLC droplets, since we did not observe the rotational flow around them. The flow field was calculated using a finite element method (see Appendix D). The size of the sphere in the simulation was set to the same value $D = 24$ μm as that in the experiments. As shown in Figs. 4(a) and 4(b), we found that the flow field around both the NLC and the CLC droplets was well reproduced by adjusting B_{01} and C_{02}. Here we set $B_{01} = -960$ μm^4/s, $C_{02} = 0$ μm^4/s for the NLC, and $B_{01} = -800$ μm^4/s, $C_{02} = -480$ μm^4/s for the CLC. The lowest order terms are sufficient to explain our experimental results. Using these parameters, we estimated the order of the chiral component of the surface flow as $|C_{02}|/(D/2)^3 = 0.3$ μm/s. In contrast, since the angular velocity of the rotating texture was $\omega \sim 0.3$ rad/s for the CLC droplets analyzed in Fig. 4,

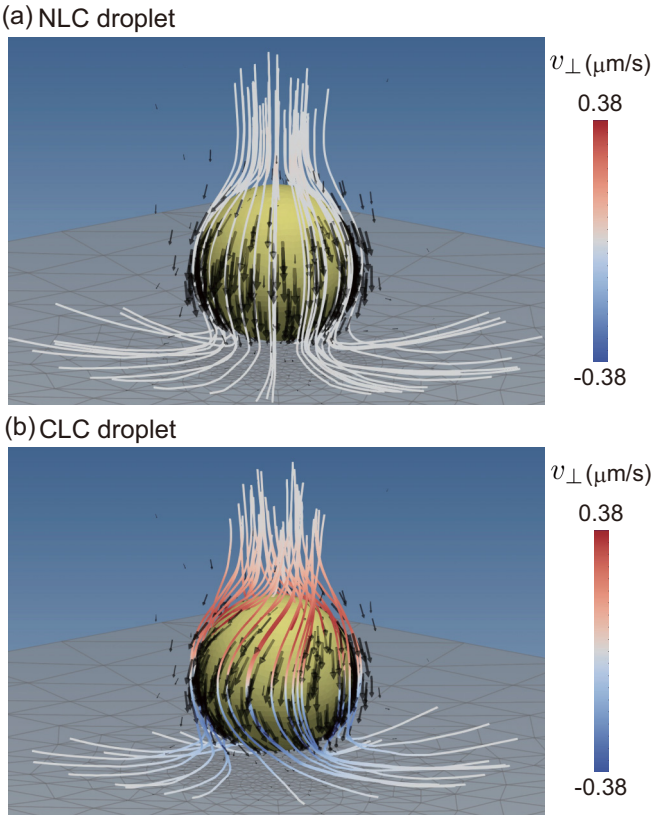

FIG. 5. 3D streamlines around (a) the NLC and (b) the CLC droplets. The streamlines were drawn for the velocity fields calculated in the numerical simulation applied in Fig. 4. The yellow spheres represent the LC droplets. The black arrows indicate the 3D velocity fields, and the size is proportional to the absolute value of the velocity field. The color of the streamlines indicates the angular component $v_\perp$ of the velocity field. The color map is also shown in each figure.

the apparent surface flow is estimated as $D\omega/2 \sim 3.6\ \mu\mathrm{m/s}$, if we assume the droplet rotates as a rigid body. Hence, the rotation of the texture is much faster than the flow field around the CLC droplets. To understand this nontrivial deviation, a future study on a numerical simulation of the hydrodynamics of the CLC will be required.

Furthermore, to characterize the flow field, we investigated the power-law behavior of the decay of the flow field around the CLC droplets [Fig. 4(c)]. With respect to the radial component, since the achiral flow is in the perpendicular direction to the wall, the profiles of the decay depend strongly on the distance z from the wall, and it was difficult to discuss the exponent of the decay. In contrast, with respect to the angular component, we found that the exponent of the decay far from the wall ($z = 18, 24, 30\ \mu\mathrm{m}$) is ~ -3 in both of the experiment and the numerical simulation. Note that this exponent -3 is consistent with that of the decay in the flow field produced by a point singularity of a rotlet dipole in the bulk [14].

III. DISCUSSION

We have presented the Marangoni-induced rotation of the CLC droplets in the surfactant solution and revealed, both experimentally and numerically, that the hydrodynamic rotlet dipole emerges around the CLC droplets. In particular, we have found that the chiral flow characterized by a rotlet dipole decays as r^{-3}, which is the same power-law behavior expected from the analytically obtained flow field around the rotlet dipole singularity. The rotation of the CLC droplets in this study is passively induced by the chiral nonequilibrium cross coupling between the rotational motion of the droplets and the flow field driven by the gravity-induced gradient of the surfactant concentration. Meanwhile, we previously reported that the CLC droplets can exhibit a self-propelled helical motion using the gradient of the surfactant concentration, when the surfactant concentration is higher [25]. Since the driving force is the same as that in this paper, we speculate that the hydrodynamic rotlet dipole also emerges around the helically self-propelled CLC droplets.

Under a torque-free condition satisfied in systems of microswimmers, a rotlet dipole is the first-order singularity in the chiral flow field. In the previous studies on swimming microorganisms exhibiting chiral motions [10,19–23], the chiral hydrodynamic flow has not been experimentally detected. Hence, our results experimentally stress the importance in measuring a flow field characterized by a rotlet dipole singularity also around swimming microorganisms, and investigating the role of a rotlet dipole on their collective behaviors.

From the viewpoint of hydrodynamics of the CLC, the rotation of the texture of the CLC droplets under some external fields (the Lehmann-type effect [33–42]) has been a long-standing unsolved problem. The spinning CLC droplet we have reported is a Lehmann-type effect driven by the surface tension gradient induced by the gradient of surfactant concentration. A Lehmann-type effect reported by Jánossy [45], where the torsional stress on the CLC drives the unidirectional diffusive flux of the particles, can be an inverse effect of our spinning CLC droplets. One of the central questions on the Lehmann-type effect is what kind of flow is generated around and inside the spinning CLC droplets. Poy and Oswald reported that no flow was observed inside the CLC droplets [40], while Yoshioka *et al.* observed the rotational flow [38]. Hence, we have no consistent experimental result for the moment. The flow measurements in these previous reports were performed on a single plane using fluorescence recovery after photobleaching. Our experiments stress that a 3D measurement of the flow field is essential since the flow field can depend on the height of the droplet. Although the mechanism of the spinning of the CLC droplets in our experiments is still being elucidated at the level of the hydrodynamics of the CLC, our studies will provide insights into the Lehmann-type effect and the hydrodynamics of the CLC as well as active matter physics.

ACKNOWLEDGMENTS

We thank K. Hirosawa and M. Shibayama for the density measurement and K. H. Nagai for carefully reading our manuscript. This work is supported by Grant-in-Aid for JSPS Fellows (Grants No. 269814 and 18J01239) and MEXT KAKENHI (Grant No. 25103004).

APPENDIX A: PRODUCTION OF MICROSCALE CLC DROPLETS AND SAMPLE PREPARATION

We used a mixture of a NLC (5CB (4-cyano-4′-pentylbiphenyl), TCI) and 2wt% of a chiral dopant (R811 or S811, WuXi AppTec Co., Ltd) as the CLC, and TTAB (tetradecyltrimethylammonium bromide, Wako) as the surfactant. To control the buoyant force exerted on the CLC droplet, H_2O was partly replaced with D_2O (Wako). The concentrations of D_2O used in Fig. 2(a) is 0wt%, 5wt%, 10wt%, 14wt%, and 18wt%, respectively. We measured the density of the CLC and TTAB solution using DMA5000s (Anton Paar). After we put a small amount of the surfactant solution on a cover glass (0.13–0.17 mm, Matsunami), a CLC droplet was injected using Femtojet (Eppendorf), a microinjector [25]. The solution was finally encapsulated with an upper cover glass using a silicon spacer (200 μm). We used an inverted optical microscope (DMI6000B, Leica) with a 40× objective (HCX PL FLUOTAR) and a CCD camera (Luca, Andor) to observe the rotating texture and measure the angular velocity. We started the calculation of the angular velocity and measured the diameter of the droplets 5 min after the injection to standardize the conditions in all the experiments. The angular velocity from three periods of rotation was calculated for each droplet.

APPENDIX B: ROTATIONAL BEHAVIOR OF THE CLC DROPLETS WITH DIFFERENT SIZE AND CHIRALITY

Here we show the rotational behaviors of the CLC droplets with different sizes (10–40 μm) and strength of chirality (5CB doped with $c_{R811} = 1, 2, 4$wt% of R811, respectively.). As shown in Fig. 6(a), we observed four types of droplets, which can be classified clearly from the textures in addition to other types of droplets ("others") which have more complicated textures with many disclinations. The first type is the "spiral droplet" we focused on in the main text. The second type, the "disclination droplet," has the texture shown in Fig. 6(b) and rotates in the CW direction (Movie S3 [27]). The director field in the disclination droplet is the same as that of the spiral droplet, while the direction of the radial disclination is perpendicular to the optical axis as depicted in Fig. 6(b). The third type is the "concentric droplet," which has a concentric texture under a natural light and a chiral fourfold texture under crossed polarizers [Fig. 6(c)]. Such concentric texture has been observed for the CLC droplets with a structure called a twisted bipolar structure (TBS) [28,30,44], where two point defects locate at the poles and the helical axis of director field is perpendicular to the line connected between the two surface defects. The rotation of the texture of the concentric droplets was not detectable due to the axial symmetry in the z direction. The fourth type is the "winding" droplet, the texture of which changes in time as shown in Fig. 6(d) (Movie S4 [27]).

When c_{R811} is relatively high ($c_{R811} = 2, 4$wt%), we observed the spiral droplets for $D < \sim 30$ μm and the disclination droplets for $D > \sim 30$ μm. The change of the stability of the two types of the droplets is beyond the scope of this paper. Nevertheless, since the only difference between the spiral and the disclination droplets is the orientation of the disclination lines, the two types should appear due to a hydrodynamic coupling between the flow inside the droplets and the director field.

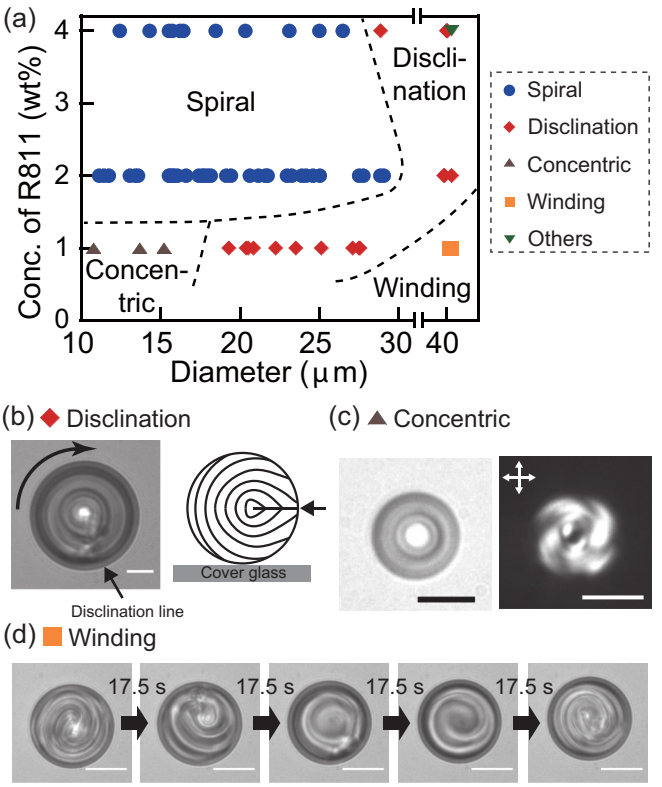

FIG. 6. Rotational behavior of the CLC droplets with different size and chirality. (a) A phase diagram of the types of the CLC droplets with the different sizes and concentration of R811. The different symbols correspond to the different types of the CLC droplets (blue circle: spiral droplet, red diamond: disclination droplet, brown upward triangle: concentric droplet, orange square: winding droplet, green downward triangle: others). The dotted curves are guides for eyes. (b) A rotating texture and the schematic cross-sectional view of the director field of a disclination droplet are shown. Arrows show the position of the disclination line. A curved arrow indicates the rotational direction. The scale bar is 10 μm. (c) A texture of a concentric droplet observed is shown. The right panel is an image obtained using cross polarizers. The direction of the polarizers is shown as the double-headed arrows. The scale bar is 10 μm. (d) A time evolution of a texture of a winding droplet is shown. The scale bar is 20 μm.

In the case of low chirality ($c_{R811} = 1$wt%), we observed the concentric, the disclination, and the winding droplets. The threshold value of D for the transition from the concentric to the disclination droplets was ~16 μm. To discuss the confinement effect on the transition, we introduce a nondimensional number $N = 2D/P$, where P is the natural pitch of the CLC. We measured P for $c_{R811} = 1$wt% using wedge cells to obtain $P = 8.6$ μm. We then calculated $N \sim 4$ for $D \sim 16$ μm. This value is consistent with a threshold value $N = 4$–8 from TBS (concentric droplet) to RSS (disclination droplet) reported in Ref. [30]. Hence, the transition should be due to the confinement effect. In contrast to the results for $c_{R811} = 2, 4$wt%, we did not observe any spiral pattern in $c_{R811} = 1$wt%. In general, the viscosity of the CLC is larger when the chirality is higher.

Hence, the flow field should be larger in the CLC droplets with the lower chirality. Such a stronger flow in the case of the low chirality $c_{R811} = 1$wt% destabilizes the spiral droplets to observe only the disclination droplets. Furthermore, we observed the winding droplets when $D \sim 40$ μm. We consider that the stronger flow expected in larger droplets dynamically disturbs the director field.

APPENDIX C: PIV EXPERIMENTS AND ANALYSIS

To calculate the hydrodynamic flow around the CLC droplets at each height, PIV analysis was performed on time-lapse images of the samples with fluorescent polystyrene beads (FluoSpheres amine-modified microspheres, yellow-green, 1.0 μm, Thermo Fisher Scientific) mixed with the TTAB solutions. Here we diluted the fluorescent beads, sold as a suspension, four times with the TTAB solution. The time-lapse images were obtained using a confocal microscope (TCS SP5, Leica) with a 40× oil immersion objective (HCX PL APO). We added 0.01wt% of a fluorescent dye BTBP [N,N-bis(2,5-di-tert-butylphenyl)-3,4,9,10-perylenedicarboximide, Sigma-Aldrich] to detect the position of the CLC droplets. The time-lapse images were taken for ∼400 s for all the droplets. The time steps Δt, the sizes $L \times L$ and the resolution R of the images were different in the *xyt* data used for Fig. 3, and the *xyzt* data used for Fig. 4: $\Delta t = 0.3$ s, $L = 201$ pix, $R = 1.7$ pix/μm for *xyt* data, and $\Delta t = 1.1$ s, $L = 101$ pix, $R = 1.0$ pix/μm for *xyzt* data.

PIV analysis was performed using mpiv.m, a free Matlab program. Before the PIV analysis, we tracked the position of the droplet using a home-made python program, and then cropped the images to locate the droplet at the center of the image, since the droplets slightly move at most within the diameter due to the inevitable global flow in the sample chamber. Then we masked the fluorescent region of the droplet with the black pixels to avoid spuriously detecting the rotation of the texture of the droplets. Using these preprocessed time-lapse images, we performed PIV analysis. We chose the size of the interrogation window as 32 pix for the *xyt* data and 8 pix for the *xyzt* data, respectively. Also, the overlaps between adjacent interrogation areas are 24 pix for the *xyt* data and 7 pix for the *xyzt* data, respectively. We subtracted the spatially averaged velocity from the obtained velocity field to eliminate the effect of the inevitable global flow inside the sample chamber. In the analysis of the radial velocity profiles as shown in Fig. 4, we eliminated the velocity vector calculated from the interrogation window overlapping the masked region with black pixels to avoid the artifact arising from such an artificial masking. Hence, the data very near the droplets are lacking. In contrast, for Fig. 3, we used the velocity vectors calculated for the interrogation window overlapping the masked pixels for visibility.

APPENDIX D: NUMERICAL CALCULATION OF VELOCITY FIELD WITH A SQUIRMER MODEL

We used FreeFem++, a free software for FEM (finite element method), to numerically solve the Stokes equation assuming the surface flow on the droplet as discussed in the main text. We put a droplet on the center of the bottom plane of a cubic bounded box with stick boundary conditions on all faces. The edge length of the cubic box is 192 μm, while the diameter of the droplet is $D = 24$ μm as observed in the PIV experiments. In the PIV experiments, we observed a layer of a few tracer particles between the droplet and the bottom glass surface. Hence, we made a small space δ between the droplet and the bottom plane. We obtained a good fit when $\delta = 3.5$ μm for both of the NLC and the CLC droplets as shown in Fig. 4. We also calculated the 3D flow fields and streamlines around the droplets shown in Fig. 5 using ParaView plugins, glyphs, and Stream Tracer.

[1] D. B. Kearns and R. Losick, Mol. Microbiol. **49**, 581 (2003).
[2] D. B. Kearns, Nat. Rev. Microbiol. **8**, 634 (2010).
[3] F. D. C. Farrell, O. Hallatschek, D. Marenduzzo, and B. Waclaw, Phys. Rev. Lett. **111**, 168101 (2013).
[4] Y. Wu, B. G. Hosu, and H. C. Berg, Proc. Natl. Acad. Sci. USA **108**, 4147 (2011).
[5] H. P. Zhang, A. Be'er, E.-L. Florin, and H. L. Swinney, Proc. Natl. Acad. Sci. USA **107**, 13626 (2010).
[6] L. Hall-Stoodley, J. W. Costerton, and P. Stoodley, Nat. Rev. Microbiol. **2**, 95 (2004).
[7] S. Park, P. M. Wolanin, E. A. Yuzbashyan, P. Silberzan, J. B. Stock, and R. H. Austin, Science **301**, 188 (2003).
[8] J. Dunkel, S. Heidenreich, K. Drescher, H. H. Wensink, M. Bär, and R. E. Goldstein, Phys. Rev. Lett. **110**, 228102 (2013).
[9] H. H. Wensink, J. Dunkel, S. Heidenreich, K. Drescher, R. E. Goldstein, H. Löwen, and J. M. Yeomans, Proc. Natl. Acad. Sci. USA **109**, 14308 (2012).
[10] E. Lauga, W. R. DiLuzio, G. M. Whitesides, and H. A. Stone, Biophys. J. **90**, 400 (2006).
[11] G. J. Hancock, Proc. Royal Soc. A **217**, 96 (1953).
[12] M. J. Lighthill, Commun. Pure Appl. Math. **5**, 109 (1952).
[13] E. Lauga and T. R. Powers, Rep. Prog. Phys. **72**, 096601 (2009).
[14] O. S. Pak and E. Lauga, J. Eng. Math. **88**, 1 (2014).
[15] A. A. Evans, T. Ishikawa, T. Yamaguchi, and E. Lauga, Phys. Fluids **23**, 111702 (2011).
[16] T. Ishikawa, J. R. Soc. Interface **6**, 815 (2009).
[17] K. Drescher, R. E. Goldstein, N. Michel, M. Polin, and I. Tuval, Phys. Rev. Lett. **105**, 168101 (2010).
[18] K. Drescher, J. Dunkel, L. H. Cisneros, S. Ganguly, and R. E. Goldstein, Proc. Natl. Acad. Sci. USA **108**, 10940 (2011).
[19] K. Drescher, K. C. Leptos, I. Tuval, T. Ishikawa, T. J. Pedley, and R. E. Goldstein, Phys. Rev. Lett. **102**, 168101 (2009).
[20] A. P. Petroff, X.-L. Wu, and A. Libchaber, Phys. Rev. Lett. **114**, 158102 (2015).
[21] J. Elgeti, U. B. Kaupp, and G. Gompper, Biophys. J. **99**, 1018 (2010).
[22] J. Gray, J. Exp. Biol. **32**, 775 (1955).
[23] J. F. Jikeli, L. Alvarez, B. M. Friedrich, L. G. Wilson, R. Pascal, R. Colin, M. Pichlo, A. Rennhack, C. Brenker, and U. B. Kaupp, Nat. Commun. **6**, 7985 (2015).

[24] E. Tjhung, M. E. Cates, and D. Marenduzzo, Proc. Natl. Acad. Sci. USA **114**, 4631 (2017).
[25] T. Yamamoto and M. Sano, Soft Matter **13**, 3328 (2017).
[26] T. Yamamoto and M. Sano, Phys. Rev. E **97**, 012607 (2018).
[27] See Supplemental Material at http://link.aps.org/supplemental/10.1103/PhysRevE.99.022704 for experimental movies.
[28] D. Seč, T. Porenta, M. Ravnik, and S. Žumer, Soft Matter **8**, 11982 (2012).
[29] E. Bukusoglu, X. Wang, Y. Zhou, J. A. Martínez-González, M. Rahimi, Q. Wang, J. J. de Pablo, and N. L. Abbott, Soft Matter **12**, 8781 (2016).
[30] P. Sleczkowski, Y. Zhou, S. Iamsaard, J. J. de Pablo, N. Katsonis, and E. Lacaze, Proc. Natl. Acad. Sci. USA **115**, 4334 (2018).
[31] S. Candau, P. L. Roy, and F. Debeauvais, Mol. Cryst. Liq. Cryst. **23**, 283 (1973).
[32] S. Herminghaus, C. C. Maass, C. Krüger, S. Thutupalli, L. Goehring, and C. Bahr, Soft Matter **10**, 7008 (2014).
[33] O. Lehmann, Ann. Phys. **2**, 649 (1900).
[34] P. Oswald and S. Pirkl, Phys. Rev. E **89**, 022509 (2014).
[35] D. Svenšek, H. Pleiner, and H. R. Brand, Phys. Rev. E **78**, 021703 (2008).
[36] P. Oswald and A. Dequidt, Phys. Rev. Lett. **100**, 217802 (2008).
[37] H. R. Brand and H. Pleiner, Phys. Rev. A **37**, 2736 (1988).
[38] J. Yoshioka, F. Ito, Y. Suzuki, H. Takahashi, H. Takizawa, and Y. Tabe, Soft Matter **10**, 5869 (2014).
[39] P. Oswald, Eur. Phys. J. E **35**, 10 (2012).
[40] G. Poy and P. Oswald, Soft Matter **12**, 2604 (2016).
[41] A. Dequidt, G. Poy, and P. Oswald, Soft Matter **12**, 7529 (2016).
[42] T. Yamamoto, M. Kuroda, and M. Sano, EPL **109**, 46001 (2015).
[43] S. R. Naganathan, S. Fürthauer, M. Nishikawa, F. Jülicher, and S. W. Grill, elife **3**, e04165 (2014).
[44] G. Posnjak, S. Čopar, and I. Muševič, Sci. Rep. **6**, 26361 (2016).
[45] I. Jánossy, J. Physique Lett. **42**, L-41 (1981).